Multiphysics modelling of lignin-derived porous electrodes for enhanced mass transport in vanadium redox flow batteries

Lwande Nontsimi [1], *Buntu* Godongwana[1], and *Myalelo* Nomnqa*[2]

[1]Department of Chemical Engineering, Faculty of Engineering and the Built Environment, Cape Peninsula University of Technology, Bellville, 7535, South Africa
[2]Department of Chemical Engineering Technology, Faculty of Engineering and the Built Environment, University of Johannesburg, Doornfontein , South Africa

Abstract. This study examines the influence of microstructure, including porosity, permeability, and tortuosity of lignin-derived electrodes (LDEs) on mass transfer behaviour in vanadium redox flow batteries (VRFBs) using a three-dimensional modelling approach. A physics-based model for the LDE was developed in COMSOL Multiphysics that couples the Navier-Stokes, Brinkman, Nernst-Planck, and Butler-Volmer equations to resolve electrolyte hydrodynamics, species transport, and electrochemical kinetics across the electrode, membrane, and flow channel domains. Model validation against published polarisation curves demonstrates strong predictive capability, with a coefficient of determination, $R^2 = 0.914$, root mean square error, RMSE = 0.0398 V, and mean absolute percentage error, MAPE ≈ 2%. In addition, hydrodynamic validation shows excellent agreement for the interdigitated flow field, $R^2 = 0.999$ and RMSE = 2.16 mbar, while the parallel configuration exhibits larger deviations, $R^2 = 0.889$ and RMSE = 31.78 mbar, highlighting limitations in capturing flow resistance. Results show that increasing porosity enhances permeability and reduces tortuosity (≈ 1.05 – 1.6), promoting uniform species distribution governed by coupled convective-diffusive-migrative transport, while improving electrochemical utilisation through more homogeneous Butler-Volmer kinetics. Furthermore, the Sherwood number increases with Reynolds number, indicating that enhanced convection associated with higher-porosity structures improves local interfacial mass transfer.

1 Introduction

The rapid expansion of renewable energy technologies such as solar photovoltaic and wind power has significantly transformed global electricity systems by reducing greenhouse gas emissions and support climate targets [1]. However, the intermittent nature of these resources presents major challenges for maintaining grid stability and reliable power supply. Solar generation is limited to daylight hours, while wind output fluctuates with atmospheric conditions, creating a growing need for efficient energy storage technologies capable of balancing supply and demand [1]. Vanadium redox flow batteries (VRFBs) have emerged as a promising solution for large-scale energy storage due to their long operational lifetimes, scalability, and improved recyclability compared with conventional lithium-ion batteries.

Despite their considerable promise for large-scale energy storage, the full realisation of VRFB technology remains limited by several significant challenges, most notably high system costs and relatively modest energy efficiency. The modelling of VRFB systems is frequently performed to investigate the influence of porous electrode microstructure on overall cell performance. Previous studies have predominantly focused on commercially available carbon-fibre-based (CFB) electrodes, including carbon felt, carbon cloth, and carbon paper [2, 3]. These materials are widely employed owing to their favourable characteristics, notably high porosity (typically in the range of 0.8-0.9), robust chemical stability, and high electronic conductivity. Notwithstanding these advantages, CFB electrodes exhibit inherent limitations, including relatively low specific surface areas and microstructural structures that are not designed to support convection-enhanced reactive transport within the porous matrix. To address these constraints, modelling approaches have been developed to investigate coupled transport phenomena, including mass transport by diffusion, convection, and migration with the hydrodynamic behaviour of the electrolyte across the 3-dimensional model [2, 3].

The performance of VRFBs is governed by mass transfer and electrochemical reactions within porous electrodes, where microstructural properties such as porosity, fibre diameter, tortuosity, and specific surface area dictate electrolyte transport pathways and reaction kinetics [3]. The modelling approach used in this model follows that of Cheng *et al.*[2], and Bordignon *et al.*[4], where the electrolyte dynamics are resolved using the Navier-Stokes and Brinkman equations for the channel flow and porous matrix, respectively, while the Nernst-Planck and Butler-Volmer equations are used to describe species and charge transport, as well as reaction kinetics. While such models have contributed significantly to understanding transport phenomena in VRFB systems, they have predominantly focused on conventional carbon-based electrodes.

Lignin-derived electrodes (LDE) have recently emerged as promising, sustainable alternatives to traditional carbon felt materials, owing to their tunable microstructural characteristics and potential for enhanced electrochemical performance [5]. To date, the influence of LDE microstructure on mass transfer behaviour remains understudied mathematically

*Corresponding author: myalelon@uj.ac.za

through modelling. The present study addresses this gap by developing a physics-based model in COMSOL Multiphysics to systematically investigate the effects of LDE microstructure on mass transport, electrolyte hydrodynamics, and electrochemical kinetics. The model further evaluates the coupled influence of operating conditions and is validated against experimental data reported by Bordignon *et al.*[4]. This study provides a more comprehensive and mechanistic understanding of structure-transport relationships beyond conventional electrode structure.

2 Model Development

2.1 Physical Model

The physical model of this study was developed in COMSOL Multiphysics® version 6.3 and is shown below:

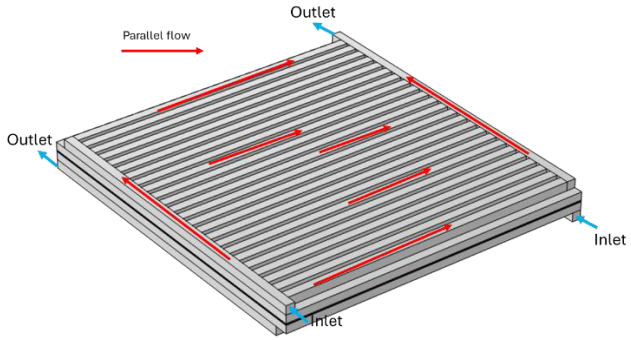

Fig. 1. A 3-Dimensional VRFB LBE with parallel flow field channel

In this system, the electrolyte first flows along the channel and subsequently through the porous electrode, where species transport occurs through the combined effects of diffusion, migration, and convection. During the charging and discharging processes, the electrochemical reactions proceed at the electrode surface as follows [6]:

$$V^{3+} + e^- \rightleftharpoons V^{2+} \quad (1)$$

$$VO^{2+} + H_2O - e^- \rightleftharpoons VO_2^+ + 2H^+ \quad (2)$$

Where the V^{3+}, V^{2+}, VO^{2+},and VO_2^+ refer to V2, V3, V4, and V5 for negative and positive half-cells reactions, respectively. The dimensions of the electrode listed in Table 1 were measured from the laboratory. The microstructural parameters such as the porosity and fibre diameter were obtained from literature reported by Hérou *et al.*[7].

2.2 Mathematical Framework

2.2.1 Model Assumptions

The model assumes steady-state, isothermal operation, with isotropic and homogeneous microstructural material properties and they were all obtained from literature reported by Hérou *et al.*[7]. The electrolyte is treated as an incompressible, Newtonian, and a dilute solution under fully developed laminar flow, while neglecting electrolyte leakage, parasitic side reactions, body forces, and gravitational effects. Within the membrane, only proton transport is considered, and crossover of other ionic species is assumed negligible [2,6,8].

2.2.2 Conservation of Mass and Momentum

The conservation of mass is governed by the continuity equation [9]:

$$\nabla \cdot \mathbf{u} = 0 \quad (3)$$

Where **u** is the electrolyte velocity vector (m/s). The conservation of momentum for the channel flow is governed by the Navier-Stokes equations [9]:

$$\rho(\mathbf{u} \cdot \nabla \mathbf{u}) = -\nabla \mathbf{p} + \mu \nabla^2 \cdot \mathbf{u} \quad (4)$$

Where ρ, μ, and **p,** are the density (kg/m^3), dynamic viscosity of the electrolyte (Pa·s) and pressure (Pa), respectively. The conservation of momentum in the porous medium is governed by the Brinkman equation [10]:

$$\frac{\rho}{\varepsilon}\left(\frac{1}{\varepsilon}(\mathbf{u} \cdot \nabla)\mathbf{u}\right) = -\nabla \mathbf{p} + \frac{\mu}{\varepsilon}\nabla^2 \mathbf{u} - \frac{\mu}{\kappa}\mathbf{u} \quad (5)$$

Where ε is the dimensionless porosity which is dimensionless and κ is the hydraulic permeability (m^2). Considering an isotropic model, the permeability is governed by [4]:

$$\kappa = \frac{d_f^2 \varepsilon^3}{16 k_{ck}(1-\varepsilon)^2} \quad (6)$$

Where d_f is the mean fibre diameter of the electrode (m) and k_{ck} is the dimensionless Kozeny-Carman constant. The porosity of the lignin-based electrode was calculated from the literature and found to be in the range of 0.4-0.93, using the following equation [7]:

$$\varepsilon = 1 - \left({}^{\rho_B}/_{\rho_T}\right) \quad (7)$$

Where ρ_B, and ρ_T represents the bulk and theoretical or apparent density.

2.2.3 Species Transport

The molar concentration profiles of the species ions, c_i (mol/dm^3) are governed by the conservation of mass:

$$\nabla \cdot \mathbf{J}_i + \mathbf{u} \cdot \nabla c_i = S_i \quad (8)$$

Where S_i are the source terms, where $i \in \{V^{2+}, V^{3+}, V^{4+}, V^{5+}, H^+,$ and $HSO_4^-\}$. The molar concentration flux, $\mathbf{J}_i$ $(mol/m^2 \cdot s)$ is given by the modified Nernst-Planck equation [11]:

$$\mathbf{J}_i = -\left(\frac{z_i c_i D_i^{eff}}{RT} F \nabla \phi_l + D_i^{eff} \nabla c_i\right) \quad (9)$$

Where z_i is the charge number, F is the Faraday's constant (96 485 C/mol), ϕ_l is the electric overpotential of the electrolyte (V), R is the gas constant (8.3145

J/mol·K), and T is the absolute operating temperature in (K). The effective diffusion given by the Bruggman correlation shown below [2]:

$$D_i^{eff} = D_i \varepsilon^{1.5} \tag{10}$$

Where the D_i^{eff} and D_i are the effective diffusion and diffusion constants (m^2/s). The source term in equation (8) is the sum of the reaction rate and dissociation rate [11]:

$$S_i = R_i + S_{d,i} \tag{11}$$

Where $S_{d,i}$ is the reaction rate, and R_i is the dissociation rate [11]:

$$R_i = \frac{\lambda_i A_V i_{loc}}{nF} \tag{12}$$

Where λ_i is the dimensionless stoichiometric coefficient of the species, A_V is the specific surface area (1/m), i_{loc} is the local current density (A/m^2), n is the charge number (n=1). The $S_{d,i}$ term is from the dissociation process of the sulfuric acid into the electrolyte which occurs in two steps shown by the following ionic reactions [2]:

$$H_2SO_4 \rightleftharpoons H^+ + HSO_4^- \tag{13}$$
$$HSO_4^- \rightleftharpoons H^+ + SO_4^{2-} \tag{14}$$

The first step is presumed complete, while the second step is modelled through the dissociation rate term governed by the following equation [11]:

$$S_{d,i} = k_d \left(\frac{c_H - c_{HSO_4}}{c_H + c_{HSO_4}} - \beta \right) \tag{15}$$

Where k_d is the dissociation rate constant and β is the HSO_4 degree of dissociation which is reported by Knehr *et al.* [12], as 0.25. The SO_4^{2-} species has been deliberately omitted as this is governed by the electroneutrality condition [11]:

$$\sum_i z_i c_i = 0 \tag{16}$$

2.2.4 Charge Conservation

The electric charge is governed by [11]:

$$\nabla \cdot (i_s + i_l) = 0 \tag{17}$$
$$i_s = -\sigma_{s,e}^{eff} \nabla \phi_s \tag{18}$$
$$\sigma_{s,e}^{eff} = \sigma_{s,e}(1-\varepsilon)^{\frac{3}{2}} \tag{19}$$
$$i_l = F \sum_i z_i \mathbf{J}_i \tag{20}$$

Where i_s is the electric current density occurring at the electrode, i_l is the ionic current density which takes place at the electrolyte, and σ_s^{eff} (S/m) is the effective electrode conductivity, which is found from the nominal electrode electronic conductivity, $\sigma_{s,e}$.

2.2.5 Electrochemical Kinetics

The electrochemical kinetics are governed by the concentration dependent extended Butler-Volmer equations. The equations for kinetics are presented in generic forms, which accounts for both the negative and positive electrodes [11]:

$$i_{loc} = i_0 \left[\frac{C_O^S}{C_O^{ref}} \exp\left(\frac{\alpha_a n F \eta}{RT}\right) - \frac{C_R^S}{C_R^{ref}} \exp\left(-\frac{\alpha_c n F \eta}{RT}\right) \right] \tag{21}$$
$$\eta = \phi_S - \phi_l - E_{eq} \tag{22}$$
$$E_{eq} = E_0 + \frac{RT}{nF} \ln\left(\frac{C_O}{C_R}\right) \tag{23}$$

Where i_0 is the exchange current density of the electrodes (A/m^2). The subscript O in the concentrations is for the oxidation which for the negative electrode is V3 and for the positive electrode it is V5. Likewise, the R subscript stands for reduction, which for the negative electrode is V2 and for positive electrode is V4. The surface concentrations shown by the superscript, S, can be found through analytical methods in literature [2, 4, 6].

2.3 Numerical Details

2.3.1 Simulation Input Parameters

Table 1. Model parameters used in the numerical simulations

Parameters	Value	References
DV2, DV3	$2.4 \times 10^{-10} m^2/s$	[2]
DV4, DV5	$3.9 \times 10^{-10} m^2/s$	[2]
DH	$9.312 \times 10^{-9} m^2/s$	[11]
$DHSO_4$	$1.330 \times 10^{-9} m^2/s$	[11]
DSO_4	$1.065 \times 10^{-9} m^2/s$	[11]
ε	0.926	[7]
d_f	$10 \mu m$	[7]
c_0	$1600 mol/m^3$	[13]
a	$29600/m$	[2]
ρ	$1430\ kg/m^3$	[2]
μ	$4.93 \times 10^{-3}\ Pa \cdot s$	[2]
$\sigma_{e,s}$	$200\ S/m$	[4]
L_e	$35\ mm$	Measured
wCell	$3\ mm$	Measured
H_{cell}	$38\ mm$	Measured
w_{ch}	$1\ mm$	Measured
H_{ch}	$1\ mm$	Measured
L_m	$183 \mu m$	Measured
i_{app}	$100\ mA \cdot c\ m^{-2}$	[4]

2.3.2 Model Verification

Model verification was conducted, as presented below:

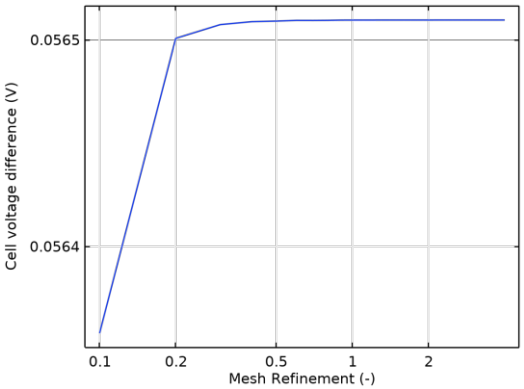

Fig. 2. Grid Independence study for the electrochemical model

The grid independence analysis in figure 2 shows that further refinement beyond 0.5 does not significantly improve accuracy. The solution reaches a plateau between meshing factor levels of 0.5 and 2.

3 Results and discussion

3.1 Model Validation

The validation of the model is a vital part of modelling, as this discerns the physical accuracy, applicability, and predictive capability. In this study, the electrochemical and CFD models were validated using the polarisation curves and pressure drops using results published by Bordignon *et al*.[4], as illustrated in figure 3.

The electrochemical model demonstrates strong predictive capability, with a high coefficient of determination, $R^2 = 0.91$, low root mean square error, RMSE = 0.0398 V and mean absolute percentage error, MAPE = 2%, confirming excellent agreement with the experimental data [4]. The statistical indicators were calculated using the following equations [14]:

$$R^2 = 1 - \frac{\sum(y_i - \hat{y}_i)^2}{\sum(y_i - \bar{y})^2} \quad (24)$$

$$\text{RMSE} = \sqrt{\frac{1}{n}\sum_{i=0}^{n}(y_i - \bar{y}_i)^2} \quad (25)$$

$$\text{MAPE} = \frac{1}{n}\sum\left|\frac{y_i - \bar{y}_i}{y_i}\right| \times 100 \quad (26)$$

For the CFD model, the interdigitated flow field (IDFF) shows very close agreement with published pressure drop data with COD of 0.999, RMSE of 2.16 mbar and MAPE of 1.44%), whereas the parallel flow field (PFF) exhibits larger deviations with COD of 0.889, RSME of 31.78 mbar, and MAPE of 15.08%, showing the underpredictions of pressure drops as the flow rates increase. This indicates that it does not capture the flow resistance as accurately. Overall, while both models show good statistical trends, the higher discrepancies in the parallel configuration suggest limitations in representing flow distribution and transport resistance compared to the more accurately resolved interdigitated case.

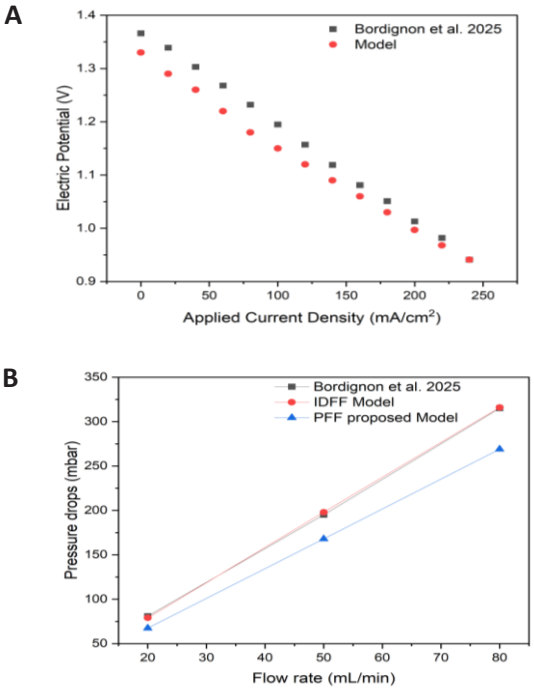

Fig. 3. Model validation results; A - Polarisation curves and B - CFD model for comparing the experimental data against the models developed

3.2 Microstructural effects on the LDE

3.2.1 Concentration distribution profiles

The concentration distribution profiles are shown in figure 4.

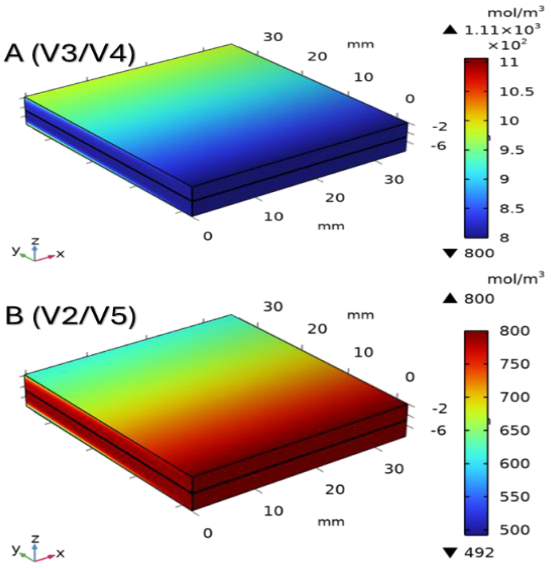

Fig. 4. A and B Species Concentration distributions at 20 mL·min^{-1} and 0.9 porosity

The species distribution in figure 4 is governed by the Nernst-Planck equation (8), where flux arises from the combined effects of diffusion, convection, and migration. In Image A, the increase in concentration from 800 to ~1000 mol·m^{-3} toward the outlet and near the current collector indicates that convective transport dominates, continuously supplying and redistributing species while reaction rates remain sufficiently moderate to avoid depletion. Conversely, Image B shows depletion to ~492 mol·m^{-3}, suggesting that diffusion-migration become limiting in balancing the convective supply. This behaviour supports the postulation that high porosity enhances permeability and effective diffusivity, promoting convective-diffusive-transport and generally minimising mass transport limitations, although localised gradients still arise due to reaction heterogeneity. These characteristics are consistent with previous studies, which report that electrode porosities approaching 0.9 minimise transport resistance while maximising accessible surface area, leading to improved electrochemical performance [4].

3.2.2 Electrode kinetics

The electrochemical behaviour is governed by the Butler-Volmer model, equation (21), coupled with charge conservation, producing spatially distributed reaction rates across the porous electrodes. The electrochemical kinetics in this study are represented by the local current density and the overpotentials shown in figure 5. The peak current density observed near the negative electrode-current collector interface arises from the imposed ground boundary condition, which maximises local overpotential and drives faster charge transfer, while the gradual decline through the electrode thickness is attributed to ohmic losses and ionic transport resistance in the electrolyte phase. At the positive electrode, the imposed discharge current constrains the distribution, resulting in moderately high but more uniform current densities near the collector interface. The corresponding overpotential field follows the same spatial trend, confirming that local reaction rates are governed by activation losses required to sustain current continuity through the porous structure. Compared to carbon felt electrodes reported by Bordignon *et al*. [4], where non-uniform current density of approximately 69 A·m^{-2}, and overpotential distributions are strongly influenced by flow field design and electrode structure, the LDE exhibits a smoother and more homogeneous electrochemical response as shown in figure 5.

This is significant because conventional carbon felt often suffers from limited kinetic reversibility and uneven reaction distribution due to its random fibrous structure and lower catalytic activity. In contrast, the more uniform profiles observed here suggest improved active site accessibility and reduced polarization, which aligns with studies showing that enhanced electrode structure leads to more uniform current distribution and lower overpotential losses. Overall, the results indicate that the LDE promotes more evenly distributed Butler-Volmer kinetics compared to traditional carbon felt, reducing localised hotspots and improving electrochemical utilisation of the electrode volume.

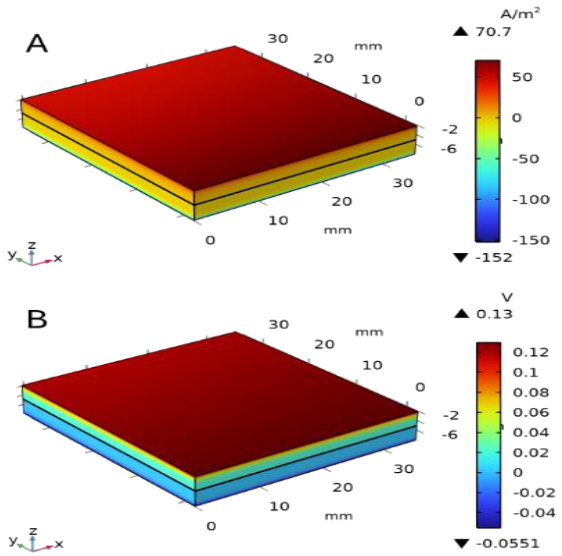

Fig. 5. Electrode kinetics at SOC of 50%, discharged at 100 mA·m^{-2}, operating at 20 ml/min

3.2.3 Permeability-Porosity relationship

The permeability-porosity relationship for the LDE is explicated by Kozeny-Carman correlation, given by equation (6), as shown in figure 6.

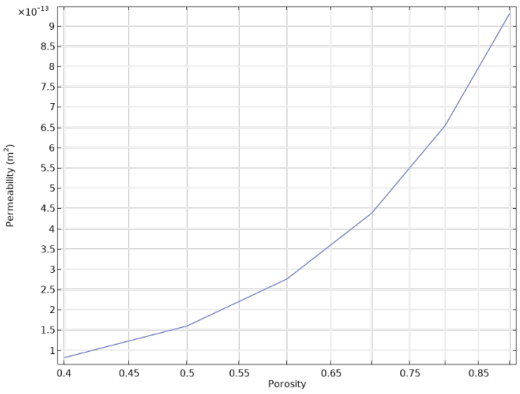

Fig. 6. Permeability-Porosity relationship for the LBE

The trend shown in figure 6 indicates that the permeability of the LDE increases with porosity, reflecting improved electrolyte transport through the porous structure. This behaviour is consistent with porous media theory, where a higher void fraction reduces hydraulic resistance and facilitates electrolyte distribution, thereby lowering the pressure drop across the electrode [3]. Although conventional carbon felt electrodes generally exhibit higher porosities and larger pore networks as reported by Ali *et al*. [3], the present results demonstrate that LDEs follow the same fundamental transport behaviour. The significance of this finding lies in the structural tunability of lignin-derived materials, which offers the potential to engineer pore structures for improved mass transport while retaining desirable mechanical and electrochemical

properties. This behaviour may be optimised through controlled electrode compression, which directly influences porosity, permeability, and electrolyte accessibility within the porous matrix.

3.2.4 Tortuosity- Porosity relationship

The relationship between the tortuosity and porosity is governed by the Bruggman correlation shown in figure 7:

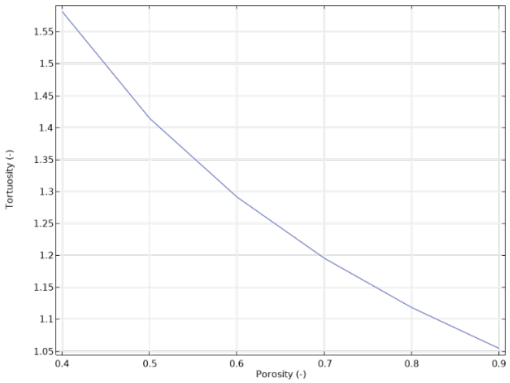

Fig. 7: Tortuosity-Porosity relationship

Tortuosity in battery electrodes typically ranges from ~1 to 3.5, with lower values indicating more direct ion transport pathways [15]. In this study, the LDE exhibits a narrow and favourable range (≈1.05–1.6) across the porosity spectrum, confirming a relatively well-connected pore network. The observed decrease in tortuosity with increasing porosity aligns with Bruggeman-type behaviour and reflects improved transport pathways at higher porosities. Compared to conventional carbon felt, this smoother and lower tortuosity profile suggests more uniform electrolyte distribution and reduced mass transfer limitations.

3.2.5 Effects of porosity on specific surface area

A key finding, consistent with both the present results and those of Ali *et al.* [3], is the inverse relationship between porosity and specific surface area. The specific surface area (SSA) of the LDE shows a decreasing trend with increasing porosity at a flow rate of 20 ml/min, reflecting the inherent trade-off between pore volume and available solid surface area per unit volume. As porosity increases, electrolyte transport and tortuosity are favoured, while SSA decreases, which affects the electrochemical reactions [3]. Therefore, an optimal porosity must be identified in the transitional region of the curve, where a balance between sufficient active surface area and adequate mass transport characteristics is achieved. This behaviour is further supported by analytical expressions that links SSA to porosity and fibre diameter, as shown below [3]:

$$a = \frac{4(1-\varepsilon)}{d_f} \tag{27}$$

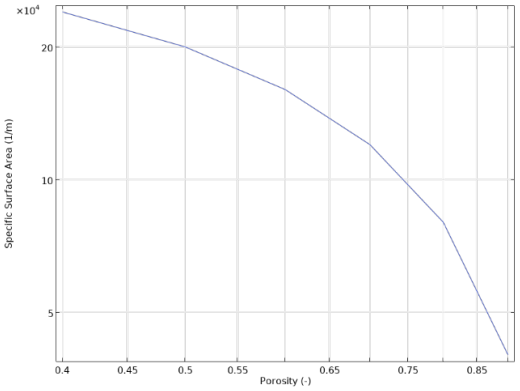

Fig. 8. Specific surface area curve vs porosity

In carbon felt electrodes, this trade-off is well established: high porosity improves transport but increases activation overpotential due to reduced reactive area [3]. However, LDEs present a notable opportunity in this regard. Their inherently hierarchical and tunable pore structures may enable higher surface area retention even at elevated porosities, particularly when derived from templated or chemically activated biomass precursors [7]. Thus, while the transport-reaction trade-off remains fundamentally unavoidable, lignin-based materials may mitigate its severity relative to conventional fibrous felts.

3.3 Mass transfer

The Sherwood number (*Sh*) is the dimensionless ratio of the convective mass transfer to diffusive mass transfer [14]:

$$Sh = \frac{k_m d_f}{D_i^{eff}} \tag{28}$$

In the present study, Sh is evaluated using the empirical correlation reported by Becker *et al.* [16]:

$$Sh = 0.07 Re^{0.66} Sc^{0.45}; 0.0018 < Re < 0.11 \tag{29}$$

Where *Re* and *Sc* are dimensionless Reynolds and Schmit numbers and this are well documented by Becker *et al.*[16]. The relationship of equation (29) is shown in figure 9.

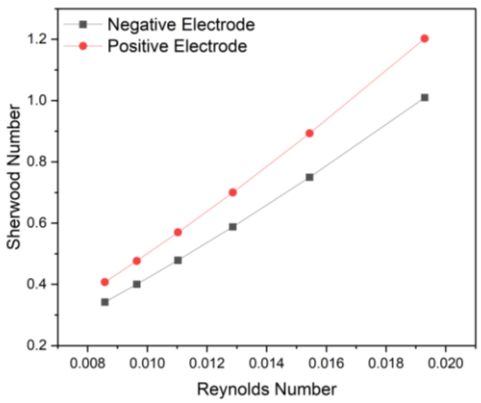

Fig. 9. Sherwood Number at different porosity, operating at 20 ml/min

At a fixed flow rate of 20 mL·min^{-1}, the results shown in figure 9 indicate that the *Sh* increases with *Re* for both the negative and positive electrodes, with the positive electrode consistently exhibiting slightly higher values across the investigated range. The source of this asymmetry lies in the *Sc* term as it is a function of diffusivity coefficient (DV2/DV3 = 1.3e-10 and DV4/DV5 = 7.74e-11). Counterintuitively, the higher Sc of the negative electrolyte species would produce a higher *Sh* through the $Sc^{0.45}$ term. The fact that the positive electrode shows higher *Sh* in figure 9 therefore suggests that differences in electrode microstructure including local porosity, fibre diameter, and specific surface area, between the two half-cells play a more significant role than the *Sc* effect alone. Importantly, the variation in *Re* arises from changes in electrode porosity rather than changes in imposed flow rate. As porosity increases from 0.4 to 0.9, the porous structure becomes more open, resulting in greater permeability and improved electrolyte penetration into the electrode. This enhances the intrinsic velocity and therefore increases the convective transport contribution represented in the *Re* of the Sherwood correlation. Consequently, the increase in *Sh* observed in figure 9 suggests that the convective mass transfer is more dominant than any corresponding increase in effective diffusion, under the present conditions. In physical terms, this implies that the higher-porosity LDE provides a more favourable transport environment for vanadium species to reach electrochemically active sites. This is an important finding, as it demonstrates that microstructural optimisation through controlled pore architecture or compression can be used to improve transport performance in VRFB operation. These results show that porosity is not merely a geometric descriptor, but a governing microstructural parameter that directly influences the balance between convection and diffusion, and therefore the mass transfer behaviour of LDEs.

3.4 Porosity on electrolyte hydrodynamics

The effects of porosity are quite evident in the pressure drops, but not in the velocity fields, shown in figure 10:

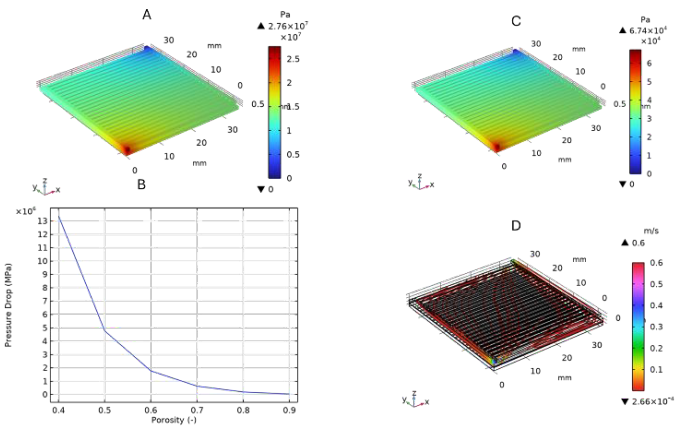

Fig. 10. CFD model results at different porosities

The pressure distribution results (A-C) show a strong dependence on electrode porosity. At low porosity (ε ≈ 0.4), the electrode exhibits significantly higher pressure drops due to reduced permeability and increased flow resistance within the compressed porous structure. This means more pumping energy is required to drive the electrolyte through the electrode, which is undesirable as it increases parasitic losses and reduces overall system efficiency. As porosity increases toward ε ≈ 0.9, the pressure drop decreases markedly (B), indicating improved permeability and easier electrolyte flow. This is favourable because it enables more uniform flow distribution and lowers the energy required for electrolyte circulation. The high-porosity case (C) therefore shows a more uniform pressure field with minimal hydraulic losses.

The velocity field (D) at ε ≈ 0.9 and 20 mL/min confirms that flow behaviour is mainly governed by the inlet channel flow rate rather than the porous matrix itself. Higher velocities are observed near the inlet region, while the rest of the domain shows a relatively smooth and uniform distribution. This suggests that at high porosity, the electrode offers minimal resistance to flow, allowing convection to dominate and enhancing mass transport. Overall, these results demonstrate that increasing porosity is beneficial for reducing pressure losses and improving electrolyte distribution, highlighting the importance of optimising the lignin-derived electrode structure for both hydraulic and electrochemical performance.

4 Conclusion

The model accurately resolves the coupled Nernst-Planck transport and Butler-Volmer kinetics in VRFB systems, demonstrating strong agreement with literature and providing mechanistic insight into LDE behaviour. Increasing porosity (ε ≈ 0.9) enhances permeability while reducing tortuosity (≈1.05-1.6), resulting in more uniform concentration fields and improved reactant accessibility, although local gradients persist due to the interplay between convection, diffusion, and reaction heterogeneity. The electrochemical response exhibits smoother current density and overpotential distributions compared to conventional carbon felt electrodes, indicating more effective utilisation of the electrochemically active surface and reduced polarisation losses. In addition, the increase in Sherwood number with Reynolds number indicates that convective mass transfer becomes more dominant as porosity increases, highlighting the strong influence of microstructure on local transport performance. These findings emphasise that microstructural tunability in LDEs provides a pathway to simultaneously reduce hydraulic losses and improve electrochemical performance, which is critical for next-generation VRFB design. Nonetheless, the present model is limited by continuum-scale assumptions, idealised morphology, and the absence of degradation and multi-physics coupling effects at the pore scale. Future work should therefore focus on multi-scale modelling approaches, rigorous experimental validation for the microstructural

properties of the LDE, and targeted optimisation of fibre structure, compression, specific surface area, and operating flow rates.

Acknowledgement

This work is based on the research supported in part by the National Research Foundation of South Africa (TTK2204112994).

Data availability

Data will be made available upon request.

References

[1] E. Sánchez-Díez, E. Ventosa, M. Guarnieri, A. Trovò, C. Flox, R. Marcilla, F. Soavi, P. Mazur, E. Aranzabe, R. Ferret, Redox flow batteries: Status and perspective towards sustainable stationary energy storage, J. Power Sources 481 (2021). https://doi.org/10.1016/j.jpowsour.2020.228804.

[2] Z. Cheng, K.M. Tenny, A. Pizzolato, A. Forner-Cuenca, V. Verda, Y.M. Chiang, F.R. Brushett, R. Behrou, Data-driven electrode parameter identification for vanadium redox flow batteries through experimental and numerical methods, Appl. Energy 279 (2020). https://doi.org/10.1016/j.apenergy.2020.115530.

[3] A. Ali, V. Ramadesigan, D.S. Monder, Modelling and simulation based impact analysis of electrode parameters on the performance of vanadium redox flow batteries, J. Power Sources 653 (2025). https://doi.org/10.1016/j.jpowsour.2025.237659.

[4] D. Bordignon, N. Zatta, A. Trovò, An extensive scaling-up oriented investigation on carbon felt flow-through and interdigitated Vanadium Flow Batteries cells, J. Power Sources 653 (2025). https://doi.org/10.1016/j.jpowsour.2025.237605.

[5] W. Li, J. Shi, Lignin-derived carbon material for electrochemical energy storage applications: Insight into the process-structure-properties-performance correlations, Front. Bioeng. Biotechnol. 11 (2023) 1121027. https://doi.org/10.3389/fbioe.2023.1121027.

[6] D. You, H. Zhang, J. Chen, A simple model for the vanadium redox battery, Electrochim. Acta 54 (2009) 6827–6836. https://doi.org/10.1016/j.electacta.2009.06.086.

[7] S. Hérou, J.J. Bailey, M. Kok, P. Schlee, R. Jervis, D.J.L. Brett, P.R. Shearing, M.C. Ribadeneyra, M. Titirici, High-Density Lignin-Derived Carbon Nanofiber Supercapacitors with Enhanced Volumetric Energy Density, Advanced Science 8 (2021). https://doi.org/10.1002/advs.202100016.

[8] M. Skyllas-Kazacos, L. Goh, Modeling of vanadium ion diffusion across the ion exchange membrane in the vanadium redox battery, J. Memb. Sci. 399–400 (2012) 43–48. https://doi.org/10.1016/j.memsci.2012.01.024.

[9] J.D. Anderson, Computational-Fluid-Dynamics-the-Basics-With-Applications-Anderson-J-D, (1995) 55–66.

[10] M.K. Das, P.P. Mukherjee, K. Muralidhar, Modeling Transport Phenomena in Porous Media with Applications, Springer International Publishing, Cham, 2018. https://doi.org/10.1007/978-3-319-69866-3.

[11] J. Newman, N. Balsara, ELECTROCHEMICAL SYSTEMS, 2021.

[12] K.W. Knehr, E. Agar, C.R. Dennison, A.R. Kalidindi, E.C. Kumbur, A Transient Vanadium Flow Battery Model Incorporating Vanadium Crossover and Water Transport through the Membrane, J. Electrochem. Soc. 159 (2012) A1446. https://doi.org/10.1149/2.017209jes.

[13] E. Ali, H. Kwon, J. Choi, J. Lee, J. Kim, H. Park, A numerical study of electrode thickness and porosity effects in all vanadium redox flow batteries, J. Energy Storage 28 (2020). https://doi.org/10.1016/j.est.2020.101208.

[14] L. Holzer, P. Marmet, M. Fingerle, A. Wiegmann, M. Neumann, V. Schmidt, Tortuosity and Microstructure Effects in Porous Media, Springer International Publishing, Cham, 2023. https://doi.org/10.1007/978-3-031-30477-4.

[15] M. Becker, T. Turek, New Mass Transport Correlation for Vanadium Redox-Flow Batteries Based on a Model-Assisted Parameter Estimation, Batteries 9 (2023). https://doi.org/10.3390/batteries9050253.